

Performance Analysis of Superconductor-constriction-Superconductor Transmon Qubits

Mingzhao Liu* and Charles T. Black

Center for Functional Nanomaterials, Brookhaven National Laboratory, Upton, NY 11973, USA

This work presents a computational analysis of a superconducting transmon qubit design, in which the superconductor-insulator-superconductor (SIS) Josephson junction is replaced by a co-planar, superconductor-constriction-superconductor (ScS) junction. For short junctions having a Kulik-Omelyanchuk current-phase relationship, we find that the ScS transmon has an improved charge dispersion compared to the SIS transmon, with a tradeoff of 50% smaller anharmonicity. These calculations provide a framework for estimating the superconductor material properties and junction dimensions needed to support proper ScS transmon operation at typical gigahertz frequencies.

I. INTRODUCTION

The transmon has become an enabling superconducting qubit device architecture, with primary advantages of immunity to charge noise and longer coherence lifetimes achieved by designing the device to have Josephson energy far exceeding the charging energy. Similar to other superconducting qubit architectures, the transmon core consists of one or more Josephson junctions (JJs), which are exclusively superconductor-insulator-superconductor tunnel junctions (SIS) – typically a thin film sandwich structure of aluminum/aluminum oxide/aluminum (Al/AIO_x/Al), in which AlO_x is the tunnel barrier (Figure 1a).

Fabrication of Al/AIO_x/Al SIS JJs typically involves physical vapor deposition of the top and bottom Al layers from two different angles relative to the substrate, through a common mask [1, 2]. After depositing the first Al layer, the sample is exposed to a controlled level of oxygen to form the thin AlO_x barrier. This ingenious fabrication method has been refined over many years but will nevertheless be highly challenging to implement at the manufacturing scale required for larger-scale quantum computers. The exponential dependence of the JJ critical supercurrent (I_c) on tunnel barrier width also results in a typical few percent variation in I_c across devices

fabricated within a few centimeters, even when oxidation conditions are tightly controlled.[3–6] Since the Josephson energy is directly proportional to I_c , this variation presents an additional design and manufacturing challenge.

In a transmon, the SIS JJ is shunted by a large capacitor to minimize the charging energy and thus provide immunity to charge noise. Further, the qubit is coupled to a high- Q microwave resonator for readout. Typically, the shunting capacitor and the resonator are fabricated separately from the SIS JJ, using a superconductor with higher T_c and better chemical robustness compared to Al (e.g., niobium ($T_c = 9.2$ K)[7], tantalum ($T_c = 4.4$ K)[8], and titanium nitride ($T_c = 5.6$ K)[9]). The improved robustness allows post-fabrication chemical treatments to remove surface contaminants, which contribute to TLS loss. However, most of these treatments are not possible after Al/AIO_x/Al junction fabrication, due to the junction's fragile nature [10].

In this work we analyze the performance impact of replacing the transmon SIS tunnel junction with a co-planar superconductor-constriction-superconductor (ScS) Josephson junction. A ScS JJ is comprised of two superconductors separated by a thin neck of the same superconductor (Figure 1b), with the constriction establishing the superconducting phase difference that enables Josephson behavior. ScS JJs are co-planar (unlike SIS tunnel junctions) and can be fabricated using conventional lithography and metallization. Here, we follow the formalism established by Koch *et al.* in [11] to determine the electrical properties of ScS transmons, which are shown to be different from SIS transmons, stemming from a different ScS JJ current-phase relationship (CPR or C Φ R) compared to that of a SIS JJ [12–14]. Comparing the two device architectures, we show that the ScS transmon has 50% less anharmonicity than the SIS transmon, for devices with the same Josephson energy and capacitive energy. However, the smaller anharmonicity is accompanied by a significantly smaller charge dispersion, giving the ScS transmon stronger immunity against charge noise.

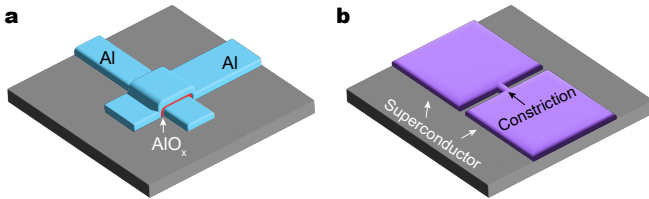


Figure 1. (a) Schematic of an Al/AIO_x/Al superconductor-insulator-superconductor (SIS) Josephson junction. For clarity, the native oxide covering both Al electrodes is omitted. (b) Schematic of a co-planar superconductor-constriction-superconductor (ScS) Josephson junction.

* mzliu@bnl.gov

II. RESULTS AND DISCUSSION

II.1. Current-phase relation of a short ScS junction

Consider a ScS Josephson junction comprised of two large superconductors connected by a diffusive quasi-one-dimensional wire with length $d \ll \sqrt{\xi_0 l}$ and width $w \ll d$, where ξ_0 is the Pippard superconducting coherence length, and $l \ll \xi_0$ is the dirty-limit electron mean free path. In this case, Kulik and Omelyanchuk showed that the CPR for the ScS junction (KO-1) at $T = 0$ K is:

$$I_{\text{ScS}}(\varphi) = \frac{\pi\Delta}{eR_n} \cos \frac{\varphi}{2} \tanh^{-1} \left(\sin \frac{\varphi}{2} \right), \quad (1)$$

in which Δ is the superconducting energy gap and R_n is the normal state resistance of the junction.[12, 13] The junction critical current $I_{c,\text{ScS}} = 0.662\pi\Delta/(eR_n)$ is achieved at $\varphi = (2k \pm 0.627)\pi$ to satisfy $dI(\varphi)/d\varphi \propto 1 - \sin(\varphi/2) \tanh^{-1}[\sin(\varphi/2)] = 0$. Given the Maclaurin series $\tanh^{-1}(x) = x + x^3/3 + O(x^5)$, Eq. 1 may be rewritten to a form that resembles the CPR of a SIS Josephson junction, as

$$I_{\text{ScS}}(\varphi) = 0.755I_{c,\text{ScS}} \sin \varphi \left[1 + \frac{1}{3} \sin^2 \frac{\varphi}{2} + O \left(\sin^4 \frac{\varphi}{2} \right) \right], \quad (2)$$

which shows that the CPR of a ScS junction distorts from the conventional sinusoidal form, but still bears odd parity and a 2π periodicity (Figure 2a).

II.2. Josephson energy of a ScS transmon

The potential energy of a Josephson junction is given by the integral:

$$E_J(\varphi) = \int I_J V dt = \int I_J \frac{\Phi_0}{2\pi} \frac{d\varphi}{dt} dt = \int I_J \frac{\Phi_0}{2\pi} d\varphi. \quad (3)$$

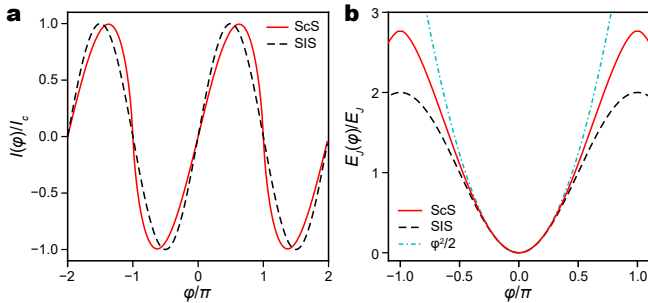


Figure 2. (a) The CPR of a ScS Josephson junction in the KO-1 limit (solid red) is distorted from the sinusoidal form of a SIS junction (dashed black). (b) The Josephson energy of a ScS transmon (solid red) deviates from the cosine form of a SIS transmon (dashed black) and has 50% smaller anharmonicity at its lowest order (φ^4). A harmonic parabola, $\varphi^2/2$, is displayed (dotted cyan) for reference.

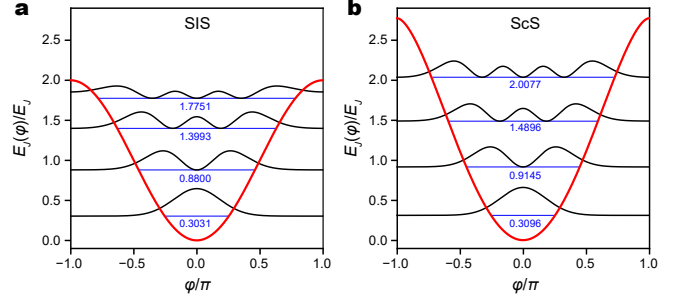


Figure 3. The eigenenergies (blue lines and numbers) and the probability densities ($\|\Psi\|^2$) of the first 4 eigenstates of (a) a SIS transmon and (b) a ScS transmon, both with $E_J/E_C = 20$ and $n_g = 1/2$. The corresponding potential energies, normalized by E_J , are plotted in red lines for both transmons.

For a short junction described by Eq. 1, the integral in Eq. 3 leads to:

$$E_{J,\text{ScS}}(\varphi) = \frac{\Delta\Phi_0}{2eR_n} \left[\ln \left(\cos^2 \frac{\varphi}{2} \right) + 2 \sin \frac{\varphi}{2} \tanh^{-1} \left(\sin \frac{\varphi}{2} \right) \right]. \quad (4)$$

Although this form appears very different from the potential energy of a SIS junction,

$$E_{J,\text{SIS}}(\varphi) = E_{J,\text{SIS}}(1 - \cos \varphi), \quad (5)$$

with $E_{J,\text{SIS}} = I_{c,\text{SIS}}\Phi_0/2\pi$, Maclaurin expansions of $E_{J,\text{ScS}}$ and $E_{J,\text{SIS}}$ make their similarities apparent:

$$E_{J,\text{ScS}}(\varphi) = \frac{\Delta\Phi_0}{4eR_n} \left(\frac{1}{2}\varphi^2 - \frac{1}{48}\varphi^4 + O(\varphi^6) \right) \quad (6)$$

$$E_{J,\text{SIS}}(\varphi) = E_{J,\text{SIS}} \left(\frac{1}{2}\varphi^2 - \frac{1}{24}\varphi^4 + O(\varphi^6) \right).$$

Comparing the coefficients of the harmonic (φ^2) term, we observe that the Josephson energy of a ScS transmon can be defined as:

$$E_{J,\text{ScS}} = \frac{\Delta\Phi_0}{4eR_n} = 0.755I_{c,\text{ScS}}\Phi_0/(2\pi), \quad (7)$$

where the last equality recognizes that $I_{c,\text{ScS}} = 0.662\pi\Delta/(eR_n)$. Eq. 7 shows that both potential energies contain anharmonicity led by a φ^4 term, from which we estimate that the anharmonicity of a ScS transmon is about *one half* that of a SIS transmon, for devices with the same E_J . This difference is clear when comparing normalized $E_J(\varphi)$ of ScS and SIS transmons with a harmonic parabolic potential $\varphi^2/2$ (Figure 2b). A more precise evaluation of the anharmonicity is given in II.3, by computing the ScS transmon eigenenergies.

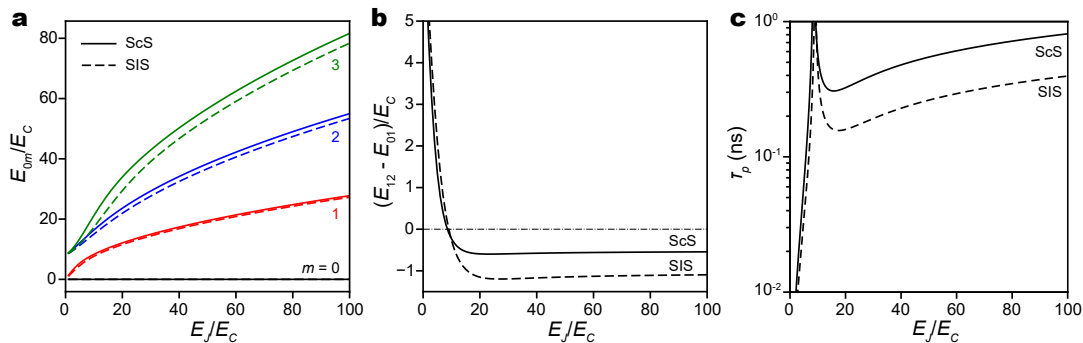


Figure 4. (a) Transition energy $E_{0m} = E_m - E_0$ at $n_g = 1/2$ and (b) oscillator anharmonicity $(E_{12} - E_{01})$ at $n_g = 1/2$, as functions of E_J/E_C for ScS transmon (solid lines) and SIS transmon (dashed lines). (c) The minimal pulse duration (τ_p) of ScS (solid line) and SIS transmons (dashed line) vs. E_J/E_C , all operated at $\omega_{01} = 2\pi \times 10$ GHz.

II.3. Eigenenergies and eigenstates of a ScS transmon

A conventional SIS transmon has a Hamiltonian of the form:

$$\hat{H}_{\text{SIS}} = 4E_C(\hat{n} - n_g)^2 + E_J(1 - \cos \hat{\varphi}), \quad (8)$$

where n_g is the offset charge. The wave equation for a SIS transmon can be solved analytically [11].

In a ScS transmon, the potential energy is given by Eq. 4, so that the Hamiltonian becomes,

$$\hat{H}_{\text{ScS}} = 4E_C(\hat{n} - n_g)^2 + E_J \left[2 \ln \left(\cos^2 \frac{\hat{\varphi}}{2} \right) + 4 \sin \frac{\hat{\varphi}}{2} \tanh^{-1} \left(\sin \frac{\hat{\varphi}}{2} \right) \right]. \quad (9)$$

The wave equation of a ScS transmon can be solved numerically using the finite difference method, in which the Hamiltonian is expressed in a discretized space of phase $\varphi \in [-\pi, \pi)$, with the periodic boundary condition applied to both ends. The validity of the computation is confirmed by comparing a similar numerical solution of the wave equation for a SIS transmon with the analytical solutions presented by Koch *et al* [11] (see also Appendix A). Figure 3 compares the first 4 eigenstates of a SIS transmon and a ScS transmon, both with $E_J/E_C = 20$ and $n_g = 1/2$. Although the lower level eigenenergies and eigenfunctions are similar, the differences become more apparent at higher energies. This trend is more clearly observed for the transition energies $E_{0m} = E_m - E_0$ calculated for both transmon types, across a range of E_J/E_C from 1 and 100 (Figure 4a). This difference reflects the smaller anharmonicity of the ScS transmon, compared to the SIS transmon. By treating the leading anharmonic term $(-\varphi^4/24)$ in Eq. 6 as a perturbation to the harmonic potential and applying the first-order perturbation theory, the m th eigenenergy of a SIS transmon

is approximated by [11]:

$$E_{m,\text{SIS}} \approx \hbar\omega_p \left(m + \frac{1}{2} \right) - \frac{E_C}{4} (2m^2 + 2m + 1), \quad (10)$$

in which $\hbar\omega_p = \sqrt{8E_J E_C}$ is the Josephson plasma energy. The transition energy between the $(m-1)$ th and m th levels is therefore

$$E_{m-1,m,\text{SIS}} \approx \hbar\omega_p - mE_C. \quad (11)$$

From Eq. 11, we find that the anharmonicity of SIS transmon, $\alpha_{\text{SIS}} \equiv E_{12,\text{SIS}} - E_{01,\text{SIS}}$, is approximately $-E_C$. By applying the same first-order perturbation theory calculation but recognizing that the perturbation term is half as a SIS transmon (Eq. 6), the m th eigenenergy of a ScS transmon can be approximated by

$$E_{m,\text{ScS}} \approx \hbar\omega_p \left(m + \frac{1}{2} \right) - \frac{E_C}{8} (2m^2 + 2m + 1), \quad (12)$$

so that its anharmonicity, α_{ScS} , is approximately $-E_C/2$, or half the anharmonicity of a SIS transmon. We can visualize this finding in a plot of numerical results, looking at transmons with $E_J/E_C \geq 20$ (Figure 4b).

The smaller anharmonicity of a ScS transmon means that the transitions E_{01} and E_{12} lie closer in energy, so that a longer RF pulse is needed to correctly excite the desired transition E_{01} . The minimal pulse duration can be estimated as $\tau_p \approx \hbar/|\alpha|^{-1}$. [11] As shown in Figure 4c, despite its lower anharmonicity, τ_p of the ScS transmon remains less than 1 ns even for $E_J/E_C = 100$, when the qubit operates at 10 GHz. Because typical qubit pulse durations are ~ 10 ns, we may conclude that the lower anharmonicity will not inhibit normal operation of a ScS transmon.

II.4. Charge dispersion of a ScS transmon

A primary benefit of the transmon architecture is its relative immunity to charge noise, when designed to operate in the regime of $E_J \gg E_C$. In a SIS transmon, the

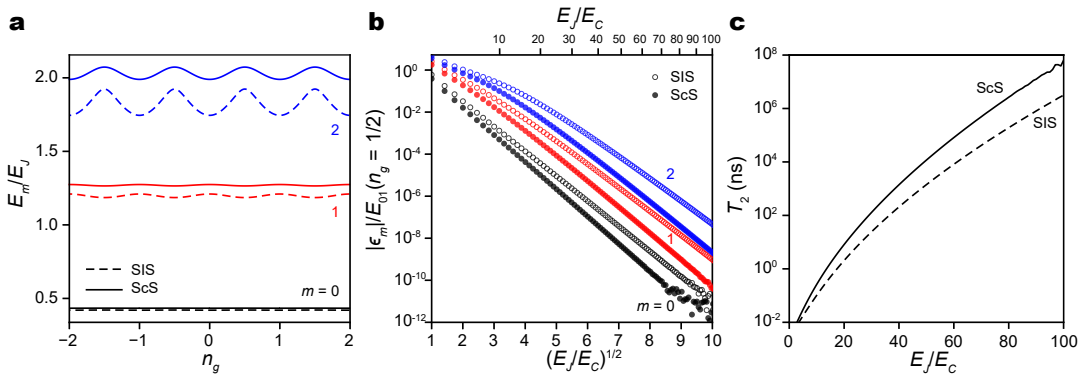


Figure 5. (a) The eigenenergies E_m of the lowest 3 eigenstates ($m = 0, 1, 2$) of a ScS transmon (solid line) and a SIS transmon (dashed lines), both with $E_J/E_C = 10$, as functions of the offset charge n_g . (b) The charge dispersion ϵ_m of the lowest 3 eigenstates of a ScS transmon (solid line) and a SIS transmon (dashed lines), as functions of E_J/E_C . (c) The dephasing time T_2 of ScS (solid line) and SIS transmons (dashed line) vs. E_J/E_C , all operated at $\omega_{01} = 2\pi \times 10$ GHz.

charge dispersion of the m th level decreases exponentially with $\sqrt{8E_J/E_C}$, following [11]:

$$\begin{aligned} \epsilon_m &\equiv E_m(n_g = 1/2) - E_m(n_g = 0) \\ &\approx E_C \frac{2^{4m+5}}{(-1)^m m!} \sqrt{\frac{2}{\pi}} \left(\frac{E_J}{2E_C}\right)^{\frac{m}{2} + \frac{3}{4}} e^{-\sqrt{8E_J/E_C}}. \end{aligned} \quad (13)$$

Intuitively, the charge dispersion is related to the tunneling probability between neighboring potential energy valleys (Figure 3), e.g., when φ makes a full 2π rotation [11]. By this reasoning, we may expect the higher barrier height of a ScS transmon ($\sim 2.8E_J$ vs. $2E_J$) to better suppress the tunneling probability and provide lower charge dispersion, compared to a SIS transmon.

Figure 5a plots the first three eigenenergies E_m ($m = 0, 1, 2$) versus the effective offset charge n_g for both SIS (dashed) and ScS (solid) transmons, with $E_J/E_C = 10$. Clearly, the ScS transmon eigenenergies are more weakly perturbed by n_g . Calculations of the charge dispersion, $\epsilon_m = E_m(n_g = 1/2) - E_m(n_g = 0)$, across a wide range of $1 \leq E_J/E_C \leq 100$ show that suppression of charge dispersion in the ScS transmon becomes more effective for larger E_J/E_C ratios (Figure 5b). When $E_J/E_C = 100$, the charge dispersion of the first excited state of a ScS transmon, $\epsilon_{1,\text{ScS}}$, is over one order of magnitude less than the corresponding SIS transmon. It is noted that computation on SIS transmon matches the analytical result very well [11], again demonstrating the high numerical precision of our finite difference computation. Nevertheless, the computational error becomes significant as the normalized charge dispersion, $|\epsilon_m|/E_{01}$, approaches 10^{-11} and smaller (see lower right corner of Figure 5b). This is due to the accumulation of floating-point error that eventually shows up for evaluating the vanishing difference between the two eigenenergies at $n_g = 0$ and $1/2$.

In Figure 5b, the y -axis is presented on a logarithmic scale and the x -axis is scales as $\sqrt{E_J/E_C}$, so that all curves take a linear form approaching large E_J/E_C values. For the SIS transmon, the slope matches the expected $\exp(-\sqrt{8E_J/E_C})$ dependence in Eq. 13. For the

ScS transmon, the slope is larger, and is best described by:

$$\epsilon_m \propto \exp\left(-\sqrt{1.16 \times 8E_J/E_C}\right).$$

The improved charge dispersion makes the ScS transmon both less sensitive to charge noise and, in turn, gives it a longer dephasing time T_2 . For dephasing caused by slow charge fluctuations of large amplitude, Koch *et al.* [11] has found an upper limit of T_2 given by:

$$T_2 \approx \frac{4\hbar}{e^2\pi|\epsilon_1|}.$$

Using this relation, we compare T_2 for both SIS and ScS transmons for E_J/E_C between 1 and 100 (Figure 5c). The ScS transmon improves T_2 across the entire range of E_J/E_C and especially at higher ratios. At $E_J/E_C = 100$, the SIS transmon has a T_2 ceiling of about 3 ms, compared to about 50 ms for the ScS transmon, an over 10 fold increase. At present, because the T_1 lifetime of SIS transmon qubits is still beyond 1 ms and not limited by the charge noise, this advantage of the ScS transmon architecture will have little performance benefit. However, because we expect the lifetimes of superconducting qubits to continue improving (*Schoelkopf's Law*) [15], there may be a point when charge noise dephasing becomes a bottleneck, for which the ScS transmon architecture can offer effective mitigation.

II.5. ScS transmon design parameters

The operational behavior of a ScS transmon is determined by its E_J and E_C , which define the operating frequency ω_{01} , the relative immunity to charge noise (ϵ_1), and the minimum excitation pulse duration (τ_p). Because these three quantities are determined by E_J and E_C , they are not independent. We can visualize this interdependence with three sets contour lines plotted in the

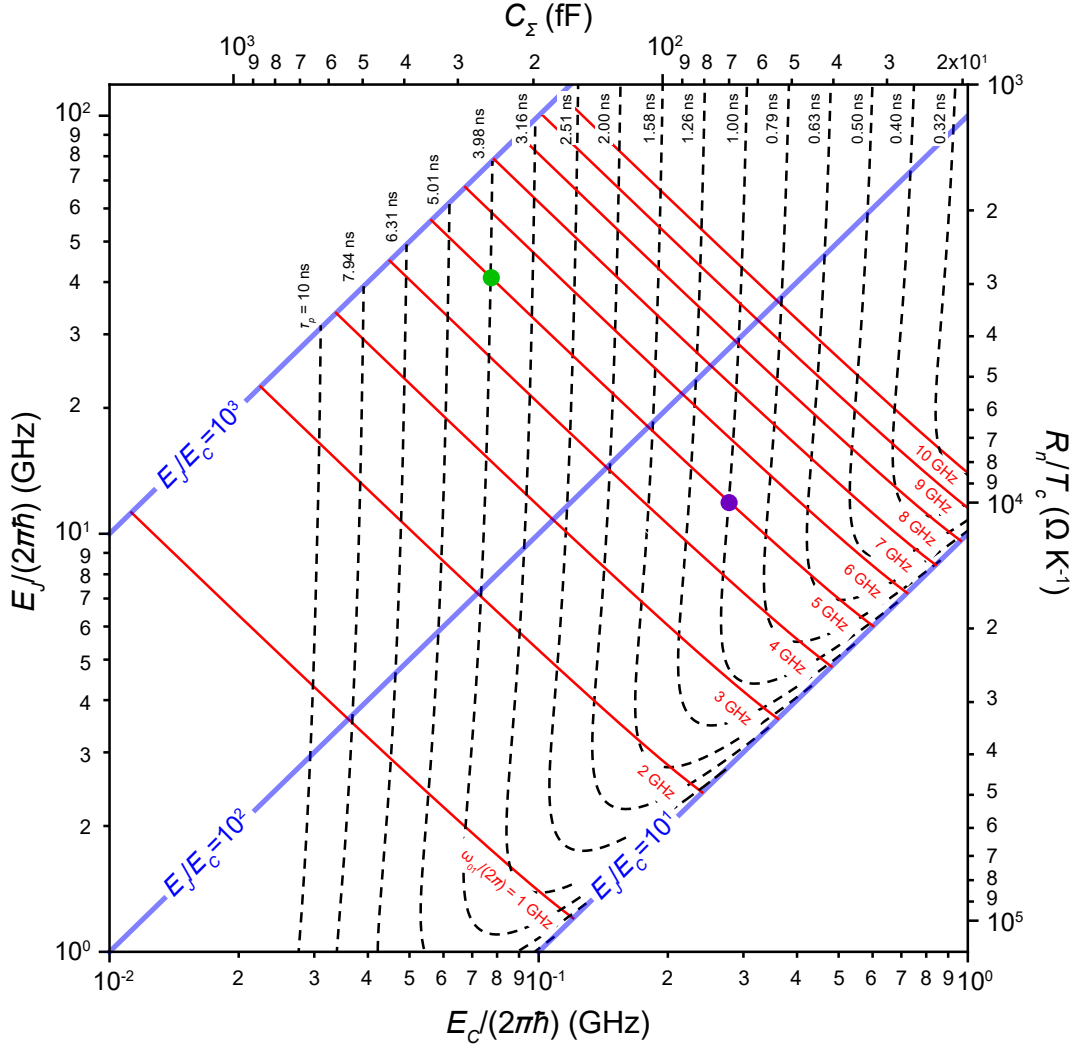


Figure 6. A graphical guide for designing ScS transmon with required E_J and E_C to match desired transmon frequency ω_{01} and minimum pulse duration τ_p . The red lines are contours lines for transmon frequencies set at values between 1 and 10 GHz. The dashed black lines are contours lines for τ_p set at a few values between 0.32 and 10 ns. The blue lines are contours lines for E_J/E_C ratios set at 10, 100, and 1000. A second x -axis that is parallel to E_C is presented for C_Σ , following $C_\Sigma = e^2/2E_C$. Similarly, a second y -axis that is parallel to E_J is presented for R_n/T_c , following $R_n/T_c = 1.76k_B\Phi_0/(4eE_J)$.

plane of E_J versus E_C (Figure 6). These contours represent: (1) a transmon operating frequency ($\omega_{01}/(2\pi)$) between 1 and 10 GHz (set of red, descending diagonal lines), (2) ratios of E_J/E_C from 10, 100, and 1000 (set of blue, ascending diagonal lines), and the minimum excitation pulse duration τ_p between 0.32 and 10 ns (set of dashed, predominantly vertical lines). Selecting two of these defines the third one. For example, a ScS transmon designed to operate at $\omega_{01}/(2\pi) = 5$ GHz and with an excitation pulse of $\tau_p = 4$ ns (green dot in Figure 6) must have a E_J/E_C ratio of about 600. Instead, a shorter excitation pulse of $\tau_p = 1$ ns (purple dot in Figure 6) requires a tradeoff of smaller $E_J/E_C \approx 40$, and thus less immunity against charge noise.

Importantly, E_J and E_C of a ScS transmon are set by the physical device dimensions and fundamental prop-

erties of the materials composing it. E_J is determined by the superconducting energy gap of the material (Δ) and the normal state resistance of the junction (R_n) (Eq. 7). For a BCS superconductor where $\Delta = 1.76k_B T_c$, we can express E_J in terms of the material properties $R_n/T_c = 1.76k_B\Phi_0/(4eE_{J,\text{ScS}})$, which is shown as the second (right) y -axis in Figure 6. Similarly, because E_C is set by the total capacitance ($C_\Sigma = e^2/2E_{C,\text{ScS}}$) which depends on device geometry and dielectric properties, we can express E_C as a capacitance, shown as a second (top) x -axis in Figure 6.

Returning to the example, we can now see from Figure 6 that designing a ScS transmon with $\omega_{01}/(2\pi) = 5$ GHz, $\tau_p = 4$ ns, and E_J/E_C ratio of about 600 (green dot) requires a junction with $R_n/T_c \approx 3 \text{ k}\Omega \cdot \text{K}^{-1}$ and capacitor with $C_\Sigma \approx 250$ fF. The properties can be realized by a

constriction junction fabricated from a thin film superconductor that has both a relatively high normal state resistivity and a long superconducting coherence length. As one example, a 10-nm-thick PtSi film has been reported with normal-state sheet resistance $R_s = 67 \Omega/\square$, superconducting $T_c = 0.63$ K, and Pippard coherence length $\xi = 440$ nm.[16] Using these material parameters, we can meet the ScS transmon design criteria using a constriction junction with physical length of 440 nm and width of 16 nm. The qubit capacitor physical dimensions should be designed for $C_\Sigma \approx 250$ fF, according to Figure 6. If one instead desires the shorter excitation pulse time of $\tau_p = 1$ ns (purple dot), the constriction must have $R_n/T_c \approx 10 \text{ k}\Omega \cdot \text{K}^{-1}$ and $C_\Sigma \approx 70$ fF. For the same PtSi superconductor, these values can be met with physical length of 440 nm and width of 5 nm. which are more challenging dimensions to fabricate.

III. CONCLUSION

In summary, we have demonstrated through computation that a short ScS Josephson junction can be used as a drop-in replacement for the SIS tunnel junction in a transmon qubit. In the transmon regime ($E_J \gg E_C$), a ScS transmon has 50% smaller anharmonicity than a SIS transmon, but appreciably lower charge dispersion that provides a significantly higher T_2 ceiling. Using this analysis, we estimate that high performance ScS transmons can be achieved with constrictions having a normal state resistance of a few kilohms, which can be made from a thin nanobridge formed in low T_c superconductors using conventional, high-resolution nanofabrication techniques. The ScS transmon design allows all components, including constriction junction, capacitor, and resonator, to be fabricated in a single lithography step. This is a significant simplification compared to multistep SIS transmon fabrication, and also provides an robust architecture amenable to device post-processing, cleaning, and encapsulation.

ACKNOWLEDGMENTS

This material is based upon work supported by the U.S. Department of Energy, Office of Science, National Quantum Information Science Research Centers, Co-design Center for Quantum Advantage (C²QA) under contract number DE-SC0012704. This research used computational resources of the Center for Functional Nanomaterials (CFN), which is a U.S. Department of Energy Office of Science User Facility, at Brookhaven National Laboratory under Contract No. DE-SC0012704.

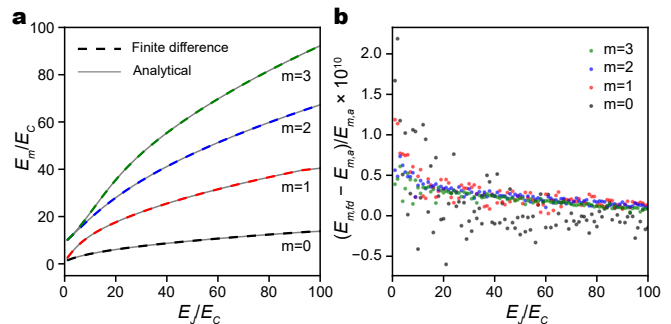


Figure 7. The first four eigenenergies of a SIS transmon, plotted versus E_J/E_C , for $n_g = 1/2$, calculated using the analytical solutions (gray solid lines) and the finite difference method (dashed lines), as functions of E_J/E_C . (b) Relative errors of the finite difference solutions, calculated as $(E_{m,fd} - E_{m,a})/E_{m,a}$, in which $E_{m,fd}$ and $E_{m,a}$ are the m th eigenenergies given by the finite difference method and the analytical solution, respectively.

Appendix A: Finite difference solutions of transmon wave equations

In the phase basis, the kinetic energies of SIS and ScS transmons are both given by

$$\begin{aligned} T &= 4E_C(\hat{n} - n_g)^2 \\ &= 4E_C \left(-\frac{d^2}{d\varphi^2} + 2in_g \frac{d}{d\varphi} + n_g^2 \right), \end{aligned} \quad (\text{A1})$$

by recognizing that $\hat{n} = -id/d\varphi$. The derivative terms can be approximated by finite differences. By discretizing φ over the interval $[-\pi, \pi)$ into an arithmetic sequence $\{\varphi_k = -\pi + k\delta\}$, where $k = 0, 1, \dots, N-1$ and $\delta = 2\pi/N$, an analytic function ψ defined over the interval is discretized as a series $\{\psi_k = \psi(\varphi_k)\}$. The first and second derivatives of ψ are approximated by finite differences to the fourth order accuracy of δ [17], as:

$$\psi^{(1)}(\varphi_k) \approx \frac{\psi_{k-2} - 8\psi_{k-1} + 8\psi_{k+1} - \psi_{k+2}}{12\delta}, \quad (\text{A2})$$

and

$$\psi^{(2)}(\varphi_k) \approx \frac{-\psi_{k-2} + 16\psi_{k-1} - 30\psi_k + 16\psi_{k+1} - \psi_{k+2}}{12\delta^2}. \quad (\text{A3})$$

In the discretized space of φ , the Hamiltonian is expressed by a $N \times N$ matrix $\mathbf{H} = \{H_{kl}\}$, ($k, l = 0, 1, \dots, N-1$), which has the following non-zero matrix elements:

$$H_{kl} = \begin{cases} \frac{E_C}{\delta^2}(10 + 4n_g^2\delta^2) + E_J(\varphi_k), & (l = k) \\ \frac{16E_C}{3\delta^2}(-1 \pm in_g\delta), & (l = (k \pm 1) \text{ mod } N) \\ \frac{E_C}{3\delta^2}(1 \mp 2in_g\delta), & (l = (k \pm 2) \text{ mod } N) \end{cases} \quad (\text{A4})$$

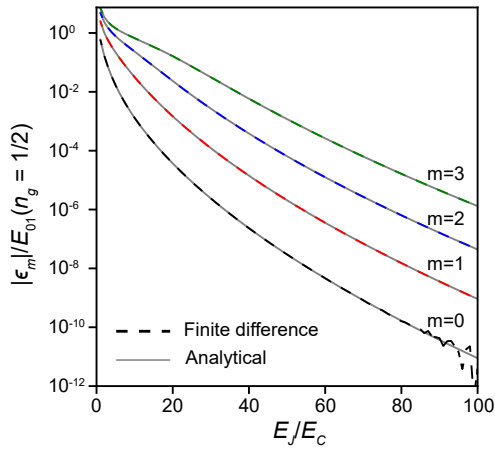


Figure 8. The charge dispersion ϵ_m of the lowest four eigenstates of a SIS transmon (dashed lines), calculated by using the analytical solutions (gray solid lines) and the finite difference method (dashed lines), as functions of E_J/E_C .

while all the other elements are 0. The $E_J(\varphi_k)$ term in the diagonal elements is the transmon potential energy and given by Eqs. 4 and 5 for ScS and SIS transmons, respectively. The modular arithmetic gives a cyclic symmetry to the off-diagonal matrix elements, which enforces the periodic boundary conditions at $\varphi = \pm\pi$.

The first few eigenvalues and eigenvectors of \mathbf{H} are obtained by using the SciPy [18] sparse matrix eigensolver (`scipy.sparse.linalg.eigs`). The validity of the finite difference method is verified by comparing the numerical results for SIS transmon with the analytical Mathieu function solutions. For the first four eigenenergies of SIS transmons with $1 \leq E_J/E_C \leq 100$ and $n_g = 1/2$, the two methods give virtually identical results (Figure 7a). The relative differences between eigenenergies obtained from the two methods are generally less than 10^{-10} , as shown in Figure 7b. The computation results on charge dispersion ϵ_m are compared in Figure 8, showing that the two methods match each other until $|\epsilon_m|/E_{01}$ reaches 10^{-11} or less, further demonstrating the accuracy of the finite difference method.

-
- [1] G. J. Dolan, Offset masks for lift-off photoprocessing, *Appl. Phys. Lett.* **31**, 337 (1977).
 - [2] T. A. Fulton and G. J. Dolan, Observation of single-electron charging effects in small tunnel junctions, *Phys. Rev. Lett.* **59**, 109 (1987).
 - [3] J. M. Kreikebaum, K. P. O'Brien, A. Morvan, and I. Siddiqi, Improving wafer-scale Josephson junction resistance variation in superconducting quantum coherent circuits, *Supercond. Sci. Technol.* **33**, 06LT02 (2020).
 - [4] J. B. Hertzberg, E. J. Zhang, S. Rosenblatt, E. Magesan, J. A. Smolin, J.-B. Yau, V. P. Adiga, M. Sandberg, M. Brink, J. M. Chow, and J. S. Orcutt, Laser-annealing Josephson junctions for yielding scaled-up superconducting quantum processors, *npj Quantum Inf.* **7**, 129 (2021).
 - [5] A. Osman, J. Simon, A. Bengtsson, S. Kosen, P. Krantz, D. P. Lozano, M. Scigliuzzo, P. Delsing, J. Bylander, and A. Fadavi Roudsari, Simplified Josephson-junction fabrication process for reproducibly high-performance superconducting qubits, *Appl. Phys. Lett.* **118**, 064002 (2021).
 - [6] H. Kim, C. Jünger, A. Morvan, E. S. Barnard, W. P. Livingston, M. V. P. Altoé, Y. Kim, C. Song, L. Chen, J. M. Kreikebaum, D. F. Ogletree, D. I. Santiago, and I. Siddiqi, Effects of laser-annealing on fixed-frequency superconducting qubits, *Appl. Phys. Lett.* **121**, 142601 (2022).
 - [7] A. Premkumar, C. Weiland, S. Hwang, B. Jäck, A. P. M. Place, I. Waluyo, A. Hunt, V. Bisogni, J. Pelliciani, A. Barbour, M. S. Miller, P. Russo, F. Camino, K. Kisslinger, X. Tong, M. S. Hybertsen, A. A. Houck, and I. Jarrige, Microscopic relaxation channels in materials for superconducting qubits, *Commun. Mater.* **2**, 72 (2021).
 - [8] A. P. M. Place, L. V. H. Rodgers, P. Mundada, B. M. Smitham, M. Fitzpatrick, Z. Leng, A. Premkumar, J. Bryon, A. Vrajitoarea, S. Sussman, G. Cheng, T. Madhavan, H. K. Babla, X. H. Le, Y. Gang, B. Jäck, A. Gye-nis, N. Yao, R. J. Cava, N. P. de Leon, and A. A. Houck, New material platform for superconducting transmon qubits with coherence times exceeding 0.3 milliseconds, *Nature Commun.* **12**, 1779 (2021).
 - [9] J. B. Chang, M. R. Vissers, A. D. Córcoles, M. Sandberg, J. Gao, D. W. Abraham, J. M. Chow, J. M. Gambetta, M. B. Rothwell, G. A. Keefe, M. Steffen, and D. P. Pappas, Improved superconducting qubit coherence using titanium nitride, *Appl. Phys. Lett.* **103**, 012602 (2013).
 - [10] K. Williams, K. Gupta, and M. Wasilik, Etch rates for micromachining processing-part ii, *J. Microelectromech. Syst.* **12**, 761 (2003).
 - [11] J. Koch, T. M. Yu, J. Gambetta, A. A. Houck, D. I. Schuster, J. Majer, A. Blais, M. H. Devoret, S. M. Girvin, and R. J. Schoelkopf, Charge-insensitive qubit design derived from the Cooper pair box, *Phys. Rev. A* **76**, 042319 (2007).
 - [12] I. O. Kulik and A. N. Omel'yanchuk, Contribution to the microscopic theory of the Josephson effect in superconducting bridges, *JETP Lett.* **21**, 96 (1975).
 - [13] A. A. Golubov, M. Y. Kupriyanov, and E. Il'ichev, The current-phase relation in Josephson junctions, *Rev. Mod. Phys.* **76**, 411 (2004).
 - [14] R. Vijay, E. M. Levenson-Falk, D. H. Slichter, and I. Siddiqi, Approaching ideal weak link behavior with three dimensional aluminum nanobridges, *Appl. Phys. Lett.* **96**, 223112 (2010).
 - [15] M. Kjaergaard, M. E. Schwartz, J. Braumüller, P. Krantz, J. I.-J. Wang, S. Gustavsson, and W. D. Oliver, Superconducting qubits: Current state of play, *Annu. Rev. Condens. Matter Phys.* **11**, 369 (2020).
 - [16] K. Oto, S. Takaoka, K. Murase, and S. Ishida, Superconductivity in PtSi ultrathin films, *J. Appl. Phys.* **76**, 5339 (1994).
 - [17] B. Fornberg, Generation of finite difference formulas on arbitrarily spaced grids, *Math. Comp.* **51**, 699 (1988).

- [18] P. Virtanen, R. Gommers, T. E. Oliphant, M. Haberland, T. Reddy, D. Cournapeau, E. Burovski, P. Peterson, W. Weckesser, J. Bright, S. J. van der Walt, M. Brett, J. Wilson, K. J. Millman, N. Mayorov, A. R. J. Nelson, E. Jones, R. Kern, E. Larson, C. J. Carey, Í. Polat, Y. Feng, E. W. Moore, J. VanderPlas, D. Laxalde, J. Perktold, R. Cimrman, I. Henriksen, E. A. Quintero, C. R. Harris, A. M. Archibald, A. H. Ribeiro, F. Pedregosa, P. van Mulbregt, and SciPy 1.0 Contributors, SciPy 1.0: Fundamental Algorithms for Scientific Computing in Python, [Nature Methods](#) **17**, 261 (2020).